Deep level transient spectroscopy of defects introduced in Si and SiGe by low energy particles

2003 J. Phys.: Condens. Matter 15 S2859

(http://iopscience.iop.org/0953-8984/15/39/011)

INSTITUTE OF PHYSICS PUBLISHING JOURNAL OF PHYSICS: CONDENSED MATTER

J. Phys.: Condens. Matter **15** (2003) S2859–S2886 PII: S0953-8984(03)67264-4

Deep level transient spectroscopy of defects introduced in Si and SiGe by low energy particles

Prakash N K Deenapanray[1] **and F Danie Auret**[2,3]

[1] Department of Electronic Materials Engineering, Research School of Physical Sciences and Engineering, The Australian National University, Canberra ACT 0200, Australia
[2] Department of Physics, University of Pretoria, Pretoria 0002, Republic of South Africa
[3] Centre for Electronic Materials, Devices and Nanostructures, UMIST, Manchester M60 1QD, UK

E-mail: pnk109@rsphysse.anu.edu.au, fauret@postino.up.ac.za and D.Auret@umist.ac.uk

Received 7 August 2003
Published 19 September 2003
Online at stacks.iop.org/JPhysCM/15/S2859

Abstract

Ion implantation and plasma processing techniques are routinely used for the fabrication of semiconductor devices. In particular, these techniques employ low energy ions, which modify the electrical and optical properties of the semiconductor material, and, consequently, of the devices that are fabricated thereon, by creating defects in the semiconductor lattice. In this paper, we review our results on the electrical characterization of defects created in Si by low energy noble gas ions (He, Ne, and Ar) and hydrogen ions using deep level transient spectroscopy. The properties of defects introduced in $Si_{1-x}Ge_x$ during ion etching and electron beam evaporation of metal contacts are also reviewed.

1. Introduction

It is well established that low energy ion bombardment creates defects in the near-surface region of semiconductors, which influence the electrical and optical properties of the crystal lattice. In particular, several device fabrication processes, including ion implantation, plasma and ion beam etching, and metallization (e.g. sputter deposition or electron beam evaporation), employ low energy ions, which modify the properties of the semiconductor material and, therefore, influence the performance of devices fabricated thereon. So, in addition to being of broad scientific interest, defect studies continue to be of prime technological importance [1]. In particular, one would like to have an intimate knowledge of the properties of defects either to avoid the deleterious effects of some (or all) or to utilize the beneficial effects of others, depending on the application. In order to fully understand the role of any defect in a particular electronic device, several properties of the defect need to be known, namely its energy level(s) in the band gap, concentration, and thermal and optical capture and emission capture cross sections for electrons and holes [2, 3]. In addition, the structure, introduction rate, introduction

and diffusion mechanisms, and thermal stability of the defect should be determined so that it can be reproducibly introduced, avoided, or eliminated, as required. It is also worth noting that the injection of point defects in low energy ion bombardment of silicon results in the pronounced relocation of subsurface doping atoms (i.e. the phenomenon of transient enhanced diffusion) [4], which limit the formation of shallow and retrograde junctions. This phenomenon makes defect studies (especially defect introduction rate and diffusion) under device processing conditions using low energy ions ever more demanding.

Deep level transient spectroscopy (DLTS) [5, 6] has been instrumental in determining most of the properties of defects introduced in several semiconductors by bombardment with different particle types and during device processing. Further, DLTS is extremely versatile because it can be used to

(a) characterize defects using a host of space-charge-based devices (e.g. Schottky barrier diodes (SBDs), p–n junctions, and more complex devices, such as field-effect transistors and metal–oxide–semiconductor devices) [7], and
(b) study the behaviour of defects in electric and magnetic fields, and under uniaxial stress [8–12] (yield structure and orientation of defects).

The latter studies can provide information about the physical structure of defects. Furthermore, the recent development of Laplace transform DLTS [12–14] has significantly increased the spectroscopic capability of conventional DLTS.

We now introduce the motivations for our studies of defects in low energy ion bombarded Si and SiGe, which fall within the overall context described above. The first section 3.2.1 of this paper discusses the electrical properties of defects introduced in n-type Si by bombardment with low energy (0.2–5 keV) noble gas ions (NGIs). NGIs with energies from 0.2 to 2 keV are routinely used during anisotropic or reactive ion etching of Si. It is, therefore, of practical importance to measure the amount of damage created in the semiconductor as a function of process parameters, such as ion energy, sputtering yield, and exposure time (i.e. ion fluence), and plasma pressure and etch rate for plasma etching [15–18]. Another equally important reason is the fact that NGI induced defects form a class of optically active defects by interacting with the intrinsic I_1 defect (the no-phonon peak at 1.018 eV) in Si [19]. Davis *et al* [20] have shown that this NGI related family of defects could be produced by bombardment of Si with 0.2–2 keV NGIs. Although the exact nature of the I_1 defect has been contested, there is a consensus that the incorporation of NGIs in the I_1 defect gives rise to deep energy levels in the band gap [20, 22–24]. Notably, deep energy levels at $E_C - 0.22$, $E_C - 0.24$ eV, and $E_V + 0.18$ eV have been reported in NGI implanted Si [25]. Apart from our studies [26–30], the investigation in [25] is, to the best of our knowledge, the only other investigation of NGI induced deep levels in silicon.

Section 3.2.2 discusses the electrical properties of defects created in n-type Si following implantation with low energy hydrogen ions [31]. The role of hydrogen in semiconductor materials cannot be overstressed. Hydrogen ions are very mobile and they exhibit a wide range of interactions with dopant impurities and lattice defects in Si. More specifically, the chemical effects of H ions can result in (a) the passivation of shallow acceptors and/or electrically active defects, and (b) the formation of H related defect complexes [32, 33]. Because it is the lightest element, implantation of hydrogen can be performed up to the ion fluences necessary to observe the chemical effects of H—a unique feature not achieved with heavier ions. Furthermore, low energy hydrogen ion bombardment of Si allows for an investigation of the trap-limited diffusion and long range migration of point defects in Si.

In section 3.3 we will discuss the electrical properties of defects created in strained p-type $Si_{1-x}Ge_x$ following low energy (0.4 keV) sputter etching [34, 35], and by electron

beam evaporation of metal contacts on the surface of the semiconductor [35, 36]. Although we have previously investigated the creation of defects in partially relaxed n-type $Si_{1-x}Ge_x$ epitaxial layers by low energy NGI bombardment [37–39], those results are not reviewed here. Recent advances in the growth of strained $Si_{1-x}Ge_x$ on graded SiGe buffer layers has led to the development of $Si_{1-x}Ge_x$/Si heterostructures with vastly improved carrier transport properties [40], which can be integrated using existing Si-based technology [41]. Furthermore, the rapid shrinking of the band gap of strained $Si_{1-x}Ge_x$ epitaxial layers with the increasing Ge mole fraction allows band gap engineering of this material, and, hence, makes it suitable for a wide range of electronic and optoelectronic device applications [42–45]. Semiconductor processes including anisotropic etching and metallization form critical steps in the fabrication of $Si_{1-x}Ge_x$-based devices. As mentioned above, bombardments with low energy NGIs during ion etching or plasma etching create defects in the semiconductor lattice. On the other hand, metallization using electron beam evaporation (EBE) is required for the deposition of metals having high melting points, and also for enhanced adhesion of metals onto the semiconductor surface. Apart from these advantages, the surface of the semiconductor material is exposed to x-rays, electrons, and heavier ions during EBE, leading to the creation of defects in the near-surface region of the semiconductor [46, 47]. Defects created in relaxed n-type $Si_{1-x}Ge_x$ by EBE have previously been investigated [48], but, to the best of our knowledge, the literature is lacking in investigations of defects created in strained $Si_{1-x}Ge_x$ layers by low energy ion bombardment. A main aim of our investigations of low energy particle induced defects in $Si_{1-x}Ge_x$ [34–39] has been to bridge this gap which exists in the literature.

2. Experimental details

2.1. Low energy NGI bombarded Si

Epitaxial Si(111) layers doped with 5×10^{15} P cm^{-3} were grown on n$^+$ substrates by chemical vapour deposition. These layers contained $\sim 10^{16}$ C cm^{-3} and $>10^{17}$ O cm^{-3}, and will hereafter be referred to as 'HOC-Si' (i.e. with high oxygen and carbon content). The epitaxial sides of samples were bombarded with 1 keV He, Ne, or Ar ions to a fluence of 1×10^{12} cm^{-2} (i.e. the number of H ions per unit area of the implanted sample) at a flux of 1×10^{11} cm^{-2} s^{-1} at room temperature. In order to investigate the influence of impurities in the creation of defects, epitaxial layers containing low concentrations of O ($<10^{16}$ cm^{-3}) and C ($\sim 10^{14}$–10^{15} cm^{-3}), and grown by CVD, were also used. This set of samples will hereafter be referred to as 'LOC-Si'. In order to compare NGI bombardment induced defects with the known point defects created by megaelectronvolt irradiation of Si, we also irradiated one set of samples with 5.4 MeV alpha particles or ^{28}Si. Self-implantation was used in order to exclude any chemical effects related to NGIs during defect creation. The fluence of alpha particles was 1×10^{12} cm^{-2} at a flux of 7.1×10^6 cm^{-2} s^{-1}, while the ^{28}Si ion fluence was 1×10^9 cm^{-2} (HOC-Si) or 2×10^{10} cm^{-2} (LOC-Si) at a flux of 1×10^9 cm^{-2} s^{-1} [26–29]. It is worthwhile noting that the nomenclature used here to distinguish between the two sets of Si samples containing different concentrations of O and C has been changed from that in [26] for better readability.

Following irradiation, the samples were chemically cleaned, and circular Pd Schottky contacts, 100 nm thick and 0.77 mm in diameter, were deposited by resistive evaporation on the bombarded surfaces. Ohmic contacts (In–Ga eutectic) were formed on the n$^+$ side of the samples prior to electrical measurements. DLTS was used to characterize the bombardment induced defects. The energy level, E_T, and apparent capture cross section, σ_a, for individual defects were determined from DLTS Arrhenius plots of $\log(e_n/T^2)$ versus $1/T$, where e_n is

Table 1. Specifications for strained p-type $Si_{1-x}Ge_x$ epitaxial layers.

Carrier density (cm^{-3})	Ge mole fraction (x)	Thickness (nm)
1.0×10^{17}	0.15	280
1.0×10^{17}	0.10	386
1.0×10^{17}	0.05	380
5.0×10^{16}	0	3000

the emission rate at a temperature T. Isochronal annealing experiments were conducted on the irradiated samples from 100 to 650 °C in steps of 50 °C under an Ar flow (zero bias) for 20 min periods. DLTS spectra were recorded after each annealing step in order to monitor the defect annealing properties and the introduction of secondary defects. Difference DLTS [49] was also used to measure the emission properties of selected electron traps under externally applied electric fields in 1 keV He ion bombarded HOC-Si annealed at 450 °C. DDLTS yields information about the defects located in a narrow spatial region, and is realized by subtracting DLTS spectra recorded at filling pulse amplitudes V_p and $V_p + \delta V_p$, using a fixed quiescent bias V_r. The effective electric field in the sample was determined by extracting the free carrier concentrations from variable-temperature capacitance–voltage (C–V) measurements. Further details about the experimental procedure can be found elsewhere [30].

2.2. Low energy hydrogen ion bombarded Si

Czochralski grown n-type Si(100) with 0.7–1.1 Ω cm resistivity was used. Samples were implanted with 7.5 keV H^+ ions to fluences, Φ, in the range 1×10^{11} cm$^{-2} \leqslant \Phi \leqslant 1 \times 10^{15}$ cm^{-2} using an ion flux $\sim 10^{11}$ cm^{-2} s^{-1} at room temperature [31]. Au Schottky contacts, 200 nm thick and 0.77 mm in diameter, were formed on the chemically cleaning surfaces after implantation. High frequency C–V measurements were used to measure the extent of free carrier compensation, while DLTS was used to probe the electrically active defects in the H^- ion implanted samples. In–Ga eutectic was used for Ohmic contact.

2.3. Processing of partially relaxed and strained $Si_{1-x}Ge_x$ epitaxial layers

Epitaxial $Si_{1-x}Ge_x$ layers grown by CVD were used. A lightly doped ($\sim$4–6 $\times 10^{16}$ cm^{-3}) Si buffer layer was first grown between 625 and 700 °C on (100) oriented p^+ substrates for p-type epilayers. The boron doping of epilayers were determined to be between 8×10^{16} cm^{-3} and 3×10^{17} cm^{-3} by C–V measurements. The specifications of $Si_{1-x}Ge_x$ epilayers are listed in table 1. The degree of strain relaxation was measured by x-ray diffraction using the (400) and (211) reflection planes for the determination of the perpendicular and parallel lattice constants, respectively.

After wet chemical cleaning, the set of p-type samples were inserted in a high vacuum system ($<10^{-8}$ mbar). Scandium contacts, 0.77 mm in diameter and 200 nm in thickness, were deposited on the epilayers through a metal contact mask, with or without a shield positioned such that no stray electrons from the electron filament were able to reach the exposed semiconductor surface. The two sets of samples (i.e. with or without electron shielding) were used to investigate the influence of stray electrons on defect creation during EBE [34, 35]. In a separate experiment, the strained p-type epilayer was sputter etched in an rf-excited (13.56 MHz) Ar plasma containing 0.4 keV ions [35, 36]. Samples were sputter etched for 5 min at a constant pressure of 5×10^{-3} mbar, with the rf electrode biased at 400 V. Ti Schottky contacts of same dimensions as above were deposited on the Ar ion etched samples using EBE

with the stray electron shielding in place. For control purposes, samples that had not undergone ion etching were metallized in parallel with the ion etched samples. The In–Ga eutectic was for Ohmic contact on the backs of the samples. DLTS was used to characterize the electrically active defects in the processed epitaxial layers. Depth profiling of defects was performed by taking the 'λ-effect' into account as proposed by Zohta and Watanabe [50].

3. Results and discussion

3.1. Low energy NGI bombarded n-type Si epitaxial layers

In this section, we discuss the electrical properties and isochronal annealing behaviour of defects created in epitaxially grown n-type Si by 1 keV He, Ne, and Ar ion bombardment, with special focus on two families of defect complexes we have labelled N1 and N3. Our semi-quantitative analysis clearly demonstrates that impurities, such as C and O, in the epilayer have a strong influence on the creation of some of these defect complexes. Evidence for the complex nature of these defects is obtained from their electric field assisted electron emission kinetics in conjunction with theoretical simulations.

3.1.1. Electronic properties of defects. Before elaborating on the results, two remarks are timely here, namely

(a) no special attempt has been made to normalize the ion fluences to generate the same nuclear energy deposited in elastic recoils for the different ions, and
(b) the defects detected by DLTS arise from the diffusion of primary defects (i.e. vacancies and interstitials) created in a volume spatially confined to the near-surface region of samples (i.e. well within the zero bias depletion layer width ∼485 nm).

TRIM simulations [51] reveal that the range, R_p, and straggling δR_p, of 1 keV He, Ne, and Ar ions in Si are (12.3, 14.0 nm), (3.8, 2.5 nm), and (3.4, 1.9 nm), respectively. Since the compensation in free carriers was less that 10% of the initial free carrier concentration (not shown), quantitative DLTS was possible. Also, quiescent bias and filling pulse conditions were chosen so that the same volume was probed during DLTS measurements.

The DLTS spectra in figure 1 are taken from HOC-Si bombarded with 1 keV He (b), Ne (c), or Ar ions (d). Spectrum (a) is obtained by 5.4 MeV alpha particle irradiation of HOC-Si. In the defect nomenclature used, 'E' denotes an electron trap, 'He or Ne or Ar' is the NGI, and the number following is the position in millielectronvolts below the conduction band edge. He or Ne ion bombardment introduced six prominent traps each, whereas Ar ions created a more complex set of defects. A comparison with spectrum (a), which identifies the point-like defects (divacancies—$V_2^{2-/-}$ and $V_2^{-/0}$, the vacancy–oxygen centre—VO, and the vacancy–phosphorus pair—VP) in megaelectronvolt alpha particle irradiated Si [52], reveals that the 1 keV NGI bombardment created the VO centre with an energy ∼0.18 eV below the conduction band edge. The DLTS peaks located at ∼80 K are due to the well-known C_i–C_s and C_s–Si_i–C_s defects [53]. The $V_2^{-/0}$ charge state of the divacancy was resolved after removing the VP pair by annealing at 200 °C for 20 min. However, the presence of $V_2^{2-/-}$ was not detected (or being in extremely low concentrations it was masked by the presence of much larger defect peaks) against spectrum (a) for the NGI bombarded samples, most probably for reasons related either to the presence of strain fields in the vicinity of the divacancy as proposed by Svensson *et al* [54], or the consumption of vacancies in the formation of vacancy clusters larger than the divacancy. Furthermore, the peak corresponding to the superposition of the VP pair and $V_2^{-/0}$

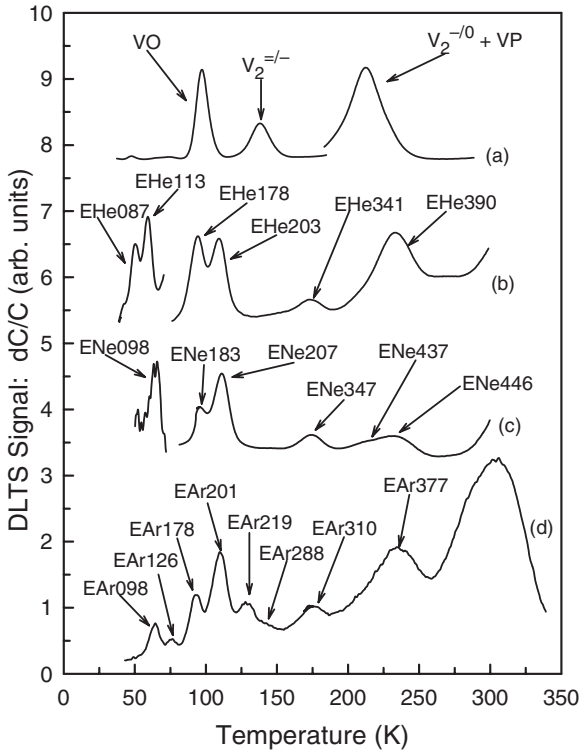

Figure 1. DLTS spectra of HOC n-type Si bombarded with: (a) 5.4 MeV alpha particles, (b) 1 keV He ions, (c) 1 keV Ne ions, and (d) 1 keV Ar ions. A fluence of 1×10^{12} cm^{-2} was used in the low energy bombardments. The spectra were recorded at a lock-in amplifier frequency of 46 Hz using a quiescent bias, $V_r = 1$ V, and a filling pulse, $V_p = 1.6$ V.

is relatively small in the 1 keV NGI bombarded sample compared to that in the 5.4 MeV alpha particle irradiated sample. These observations would support the suggestion that vacancies produced in the low energy NGI bombarded samples are predominantly trapped in clusters larger than the divacancy and by oxygen interstitial, O_i [55], to form the VO centre. In addition, the presence of more intense defects peaks at the higher temperatures, which we are unable to identify, mask the smaller (VP + $V_2^{-/0}$) defect peaks in the low energy ion bombarded samples. We have observed a set of prominent defect peaks located at ∼110 K (figure 1) in the NGI bombarded samples—EHe203, ENe207, and EAr201—and have assigned them to the same family of defects, N1. We have also grouped defect peaks EHe310, ENe347, and EAr341 at ∼175 K into another family of defects, N2. Although we have not performed any stringent characterization of the N2 defects, we speculate that they could be related to the hydrogen related VO–H complex [31].

The 'signatures' (i.e. energy level, E_T, and apparent capture cross section, σ_a), of the prominent electron traps were determined from DLTS Arrhenius plots of $\log(e_n/T^2)$ versus $1/T$ [26], and are summarized in table 2. DLTS peaks which have similar 'signatures' and annealing behaviours are listed in the last column of table 2. Since some defect peaks overlap, it was difficult to determine the energy positions of such peaks accurately. Figure 2 captures the relationship between the defects created in HOC-Si by 1 keV NGI bombardment. The tentative identification of the defects is also given. Of greater interest are the two families of

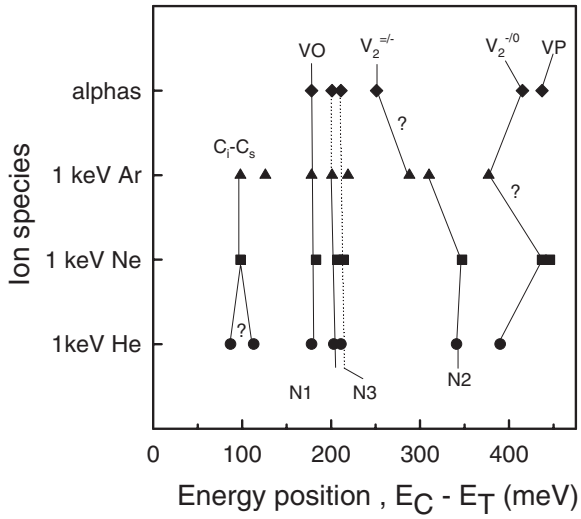

Figure 2. A schematic diagram illustrating the relationship between the defects introduced by 1 keV He, Ne, Ar ion bombarded HOC n-type Si, and the point-like defects created by 5.4 MeV alpha particle irradiated HOC n-type Si. Three new families (N1, N2, and N3) of similarly structured defects are depicted. The 'N3' defects are introduced at the expense of the 'N1' defects by annealing above 300 °C (dotted line). Defects belonging to N1 and N3 are proposed to be complex vacancy clusters, while the 'N2' defects could be similar to previously reported hydrogen related complexes.

defects labelled N1 and N2 in the as-irradiated samples, which cannot be attributed to point-like defects (spectrum (a) in figure 1). Figure 2 also shows that a third family of secondary defects, N3, is created in the NGI bombarded samples by annealing above 350 °C (see section 3.1.2). Our forthcoming discussion will be predominantly on the N1 and N3 families of defects, since these defects either have not been detected in previous studies or have not received much discussion in the literature. We will demonstrate that N1 and N3 constitute vacancy clusters that are larger than the divacancy.

In order to explain why 1 keV NGIs create different sets of defects compared to 5.4 MeV alpha particles (i.e. point defects), the energy loss mechanisms of these ions has to be considered. 5.4 MeV alpha particles lose their energy predominantly by electronic stopping in the first $\sim$20 μm of their $\sim$26 μm range and, therefore, create little structural damage in the region probed by DLTS in this study. A large fraction of the Frenkel-type defects—single vacancies, V, and self-interstitials, Si_i—annihilate via surface enhanced recombination [54]. The remaining fast diffusing single vacancies are either trapped by impurities such as O_i and P to form VO and VP pairs, or combine to form divacancies, V_2 (curve (a) in figure 1). The displaced lattice atoms (self-interstitials) are predominantly annihilated via recombination with vacancies or diffuse. Abdullin *et al* [56] have shown that Si_i introduced two energy levels at $E_C - 0.39$ eV ($Si_i^{0/+}$—the neutral state of Si_i) and $E_C - 0.25$ eV ($Si_i^{+/2+}$) in Cz and FZ p-type Si irradiated with 4.7 MeV alpha particles. The latter level is observed only after minority carrier injection using optical excitation. However, these levels are not detected in n-type Si because the neutral state of Si_i is ionized, and anneals around 160–170 K owing to thermal charge transfer. Furthermore, a small fraction of remaining Si_i may interact with C_s to form the C related defects, C_i–C_s and C_s–Si_i–C_s. The formation of the C_i–C_s proceeds by the intermediate reaction $Si_i + C_s \rightarrow C_i$ [53]. On the other hand, the low energy NGIs lose their energy predominantly by nuclear stopping on entering the Si lattice. In this low energy

Table 2. Properties of defects introduced by 1 keV NGIs, and 5.4 meV alpha particles in HOC-Si.

Ion and energy	Defect	E_T (meV)	σ_a (cm^2)	T_{peak} [a] (K)	Similar defects
He: 1 keV	EHe087	87 ± 2	8.2×10^{-16}	51	
	EHe113	113 ± 2	3.6×10^{-15}	60	C_i–C_s
	EHe178	178 ± 2	7.5×10^{-16}	93	VO
	EHe203	203 ± 3	1.1×10^{-15}	108	EAr201/ENe207
	EHe341	341 ± 4	1.0×10^{-15}	176	EAr310/ENe347
	EHe390	390 ± 4	6.3×10^{-17}	225	EAr377?
Ne: 1 keV	ENe098	98 ± 2	4.4×10^{-17}	65	C_i–C_s
	ENe183	183 ± 2	1.8×10^{-15}	94	VO
	ENe207	207 ± 3	4.8×10^{-15}	109	EHe203/EAr201
	ENe347	347 ± 4	1.9×10^{-15}	174	EHe341/EAr310
	ENe437	437 ± 5	4.5×10^{-15}	208	VP?
	ENe446	446 ± 5	4.4×10^{-16}	232	
Ar: 1 keV	EAr098	98 ± 2	6.6×10^{-17}	64	C_i–C_s
	EAr126	126 ± 2	2.2×10^{-16}	76	
	EAr178	178 ± 2	7.5×10^{-16}	93	VO
	EAr201	201 ± 3	9.7×10^{-16}	108	EHe203/ENe207
	EAr219	219 ± 4	1.4×10^{-16}	128	
	EAr288	288 ± 4	1.1×10^{-15}	149	
	EAr310	310 ± 4	1.6×10^{-16}	174	EHe341/ENe347
	EAr377	377 ± 5	1.1×10^{-17}	235	EHe390?
He: 5.4 MeV	Eα178	178 ± 2	7.5×10^{-16}	93	VO
	Eα251	251 ± 3	1.3×10^{-15}	131	$V_2^{2-/-}$
	Eα415	415 ± 4	1.9×10^{-16}	226	$V_2^{-/0}$
	Eα437	437 ± 4	2.4×10^{-15}	217	VP

[a] The peak temperature at a lock-in amplifier frequency of 46 Hz, i.e. a decay time constant of 9.23 ms.

regime, the collision cascades are much denser so the trajectory of an ion is characterized by large vacancy aggregates [57]. The vacancy clusters are created either by the combination of several single vacancies trapped in the highly damaged area or in single events. The structures of the defects created during 1 keV NGI bombardment are, thus, expected to be more complex than those of the primary point defects observed after 5.4 MeV alpha particle irradiation.

In addition to the non-detection of V_2 and VP in the low energy NGI bombarded HOC-Si, a further observation can be made from figure 1 which suggests that the N1 defects are most probably complex vacancy clusters. Since the nuclear component of energy deposited by 1 keV NGI in Si increases with ion mass, it can be expected that more higher order vacancy clusters will be produced compared to primary point defects (VO centres and V_2) when bombarding with the heavier NGIs. The fact that the relative DLTS intensity of the VO centre compared to the N1 defect is found to decrease by $\sim$5 times with the increasing mass of the noble gas species reveals the complex nature of EHe203, ENe207, and EAr201. A similar effect has also been observed in HOC-Si bombarded with different fluences of 1 keV Ar ions [58]. The density of collision cascades increases with the increasing ion fluence, resulting in the creation of complex defects.

We now demonstrate the influence of NGI bombardment of LOC-Si. Three prominent electron traps EHe201, EHe296, and EHe554 are created in 1 keV He ion bombarded LOC-Si

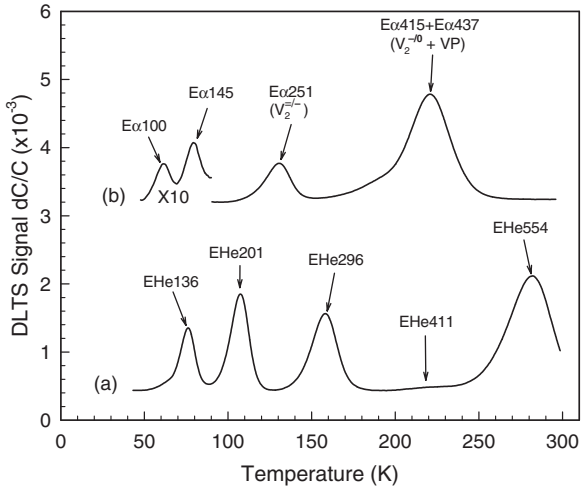

Figure 3. DLTS spectra of 1 keV (curve (a)) and 5.4 MeV (curve (b)) He ion irradiated LOC n-type Si. Spectra were recorded at a lock-in frequency of 46 Hz, $V_r = 0.5$ V and $V_p = 0.5$ V.

Table 3. Properties of defects created in 1 keV He ion bombarded LOC-Si.

Defect	E_T (meV)	σ_a (cm^2)	T_{peak} [a] (K)	$N_T(0)$ (cm^{-3})	L (nm)	Similar defects	T_{out} [b] (°C)
EHe136	136 ± 2	6.5×10^{-16}	77	3.0×10^{15}	29		300
EHe201	201 ± 3	1.2×10^{-15}	107	1.6×10^{16}	23	N1	500
EHe296	296 ± 3	5.8×10^{-16}	158	1.1×10^{16}	25	N2	400
EHe411	411 ± 4	1.4×10^{-16}	226			VP?	180
EHe554	554 ± 4	5.8×10^{-16}	281	1.1×10^{16}	21		500

[a] The peak temperature at a lock-in amplifier frequency of 46 Hz, i.e. a decay time constant of 9.23 ms.
[b] The temperature at which the defect was removed after isochronal (15 min periods) annealing.

as illustrated by the bottom curve in figure 3 [28]. The upper spectrum in figure 3 is taken from the 5.4 MeV alpha particle irradiated sample. Similar to the situation depicted in figure 1, the presence of V_2 and VP pairs is not detected in the low energy bombarded sample, despite the fact that the P doping level is six times higher than in HOC-Si and the significantly lower concentration of O_i in LOC-Si. The VO centre is not detected in the ion bombarded LOC-Si sample. These observations concerning the non-detection of point defects in the O-poor Si sample add more weight to our previous suggestion that the defects created by low energy NGIs are complex vacancy defects. The properties of the defects are summarized in table 3. EHe201 in LOC-Si is similar to EHe203 in HOC-Si. EHe554 could also be present in HOC-Si, but cannot be resolved as it is masked by EHe390 and a prominent defect peak above 300 K (identified as EHe584 in figure 4). DLTS depth profiling was used to measure the distribution of the defects. The concentration of defects decreased exponentially from $\sim 10^{14}$ cm^{-3} at $\sim$100 nm below the surface to $\sim 10^{12}$ cm^{-3} beyond 0.22 μm from the surface [28]. The characteristic diffusion length, L, together with the extrapolated surface concentration, $N_T(0)$, of the prominent electron traps are also listed in table 3. Of particular interest in table 3 are the extremely low values of L between 21 and 25 nm of the defects EHe201, EHe296, and EHe554, which could be characteristic of large defect clusters with very low mobility. However, another

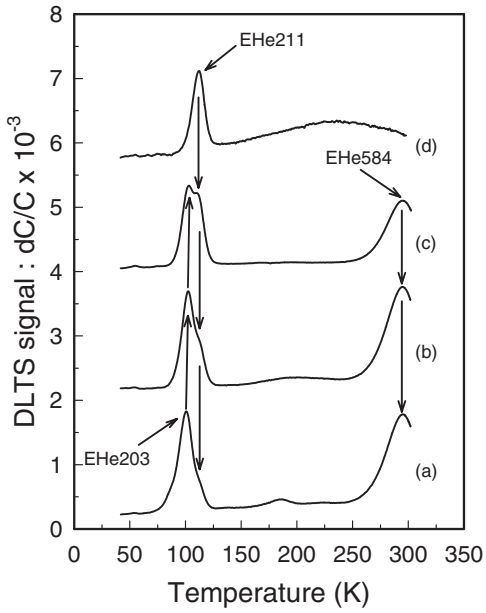

Figure 4. (a) Isochronal annealing behaviour of dominant electron traps in He ion bombarded HOC n-type Si. Spectra (a) to (d) correspond to annealing temperatures of 350, 450, 500, and 650 °C, respectively. Samples were annealed for 20 min periods under an Ar flow and zero bias, and the spectra were recorded at a lock-in frequency of 10 Hz.

important point should be borne in mind regarding defects created by low energy NGIs. These ions may become incorporated into vacancy clusters as discussed in the introduction to form a class of optically active NGI related defects [19–22]. The theoretical studies of Estreicher *et al* [23, 24] have shown that the most stable vacancy cluster for the formation of this class of NGI related defects was the neutral charge state of V_2. Hence, the non-detection or extremely low concentrations of V_2 is our 1 keV NGI bombarded samples could also be due to the chemical interaction between NGIs and V_2.

3.1.2. Isochronal annealing behaviour. A comparison of the isochronal annealing behaviour of defects created in our n-type Si epilayers by either low energy NGIs or by 5.4 MeV ^{28}Si provides evidence for the formation of vacancy clusters larger than V_2 in the low energy NGI bombarded samples.

Curves (a)–(d) in figure 4 depict the DLTS spectra of 1 keV He ion bombarded HOC-Si after annealing at 350, 450, 500, or 650 °C, respectively, while figure 5 shows the DLTS spectra of Ar (LIA frequency of 46 Hz) and Ne (LIA frequency of 10 Hz) bombarded HOC-Si annealed at 400 or 550 °C. A lower peak position of EHe203 and ENe207 at ∼105 K is due to the use of an LIA frequency of 10 Hz in figures 4 and 5 (compared to ∼110 K at 46 Hz in figure 1 and table 1). These isochronal annealing experiments show that the defect with a DLTS peak at ∼110 K (LIA frequency of 46 Hz) is stable up to ∼450 °C. In this temperature range, a set of secondary defects, N3, with energy levels at $E_C - 0.211$ eV (EHe211), $E_C - 0.214$ eV (ENe214), and $E_C - 0.219$ eV (EAr219) emerges in the annealed samples. Spectra (a)–(c) in figure 4 also show that 1 keV He ion bombardment of HOC-Si introduces a defect EHe584, which appears to have similar thermal properties to EHe203. The similarity between the

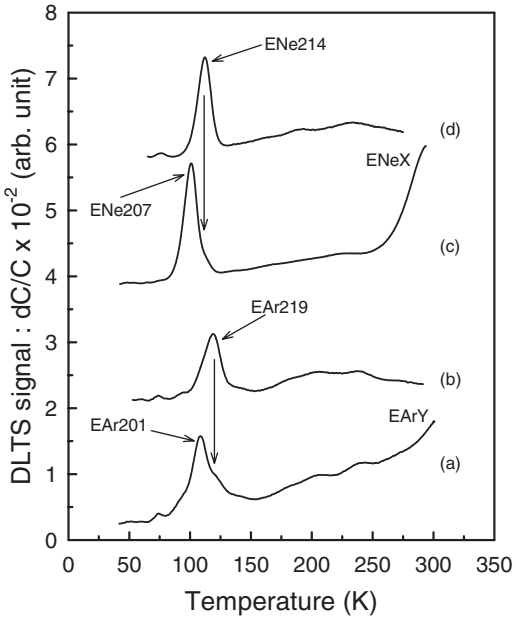

Figure 5. DLTS spectra of 1 keV Ar and Ne ion bombarded HOC n-type Si corresponding to annealing temperatures of 400 °C (curves (a) and (c)) and 550 °C (curves (b) and (d)). Lock-in amplifier frequencies of 46 and 10 Hz were employed to obtain the Ar and Ne spectra, respectively.

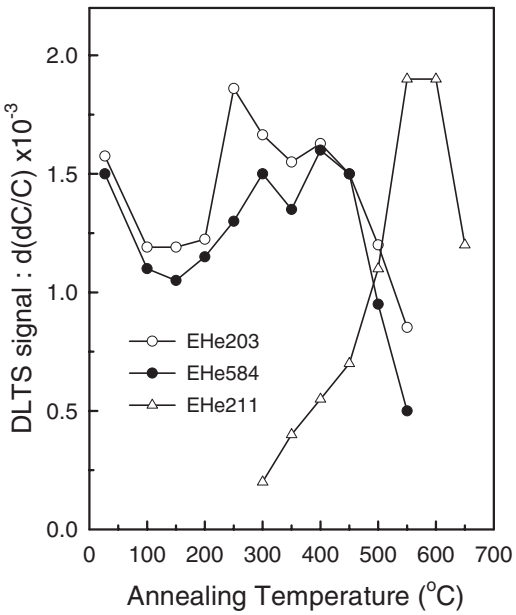

Figure 6. Variation of the peak DLTS intensities for EHe203, EHe584, and EHe211 as a function of isochronal annealing temperature. The fading EHe203 peak above 550 °C is masked by the intense EHe211 peak. The peak intensity of EHe584 could not be measured above 550 °C because of the broad and skewed baseline of the DLTS spectra above 200 K. The annealing behaviours of EHe203 and EHe584 are quite similar, and the creation of EHe211 occurs at their expense.

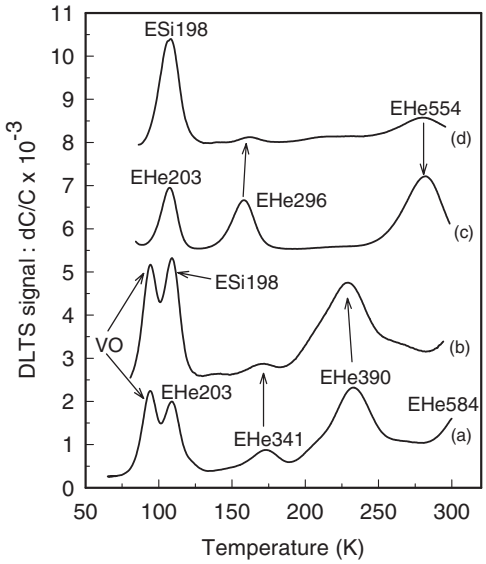

Figure 7. DLTS spectra of: (curve (a)) 1 keV He ion bombarded HOC n-type Si, (curve (c)) 1 keV He ion bombarded LOC-Si, and 5.4 MeV $^{28}Si^{4+}$ implanted HOC n-type Si (curve (b)) and LOC-Si (curve (d)). The spectra were recorded using a lock-in amplifier frequency of 46 Hz.

thermal stabilities of EHe203 and EHe584 is clearly illustrated in figure 6. The DLTS peak of EHe584 is not seen in figure 1(b) since its peak position is above 300 K for an LIA frequency of 46 Hz. The broad peak seen at high temperature in figure 4(d) could be caused by either the degraded metal–semiconductor interface at 650 °C or the presence of extended defects which introduce a continuous band of defects in the band gap [59].

Spectra (a) and (c) in figure 5 show a high temperature shoulder on the DLTS peak at ∼110 K (i.e. N1) indicative of a secondary peak, in Ar and Ne ion bombarded HOC-Si samples annealed at 400 °C, respectively. This latter defect peak (i.e. for N3) is fully resolved after annealing at 500 °C, and its intensity is also observed to increase with the disappearance of the N1 defects. Furthermore, figure 5(c) reveals that Ne ion bombarded HOC-Si contains a defect labelled ENeX, which has similar annealing characteristics to EHe584. Since the peak temperature of ENeX is almost the same as that for EHe584, it is possible that they are structurally similar. The same argument may hold for defect EArY created in the sample bombarded with Ar ions. ENeX and EArY could indeed be similar defects to EHe584, since their isochronal annealings are similar to that demonstrated in figure 6 for the He bombarded sample. Hence, EHe584, ENeX, and EArY could well constitute yet another family of defects, N4. However, further experimental evidence would be required before for this claim could be verified, since we have not undertaken full characterization of ENeX and EArY.

Figure 7 illustrates the DLTS spectra taken from 1 keV He ion bombarded HOC-Si and LOC-Si (curves (a) and (c)), as well as the spectra from 5.4 MeV Si implanted HOC-Si and LOC-Si (curves (b) and (d)). It is pointed out here that curve (c) is similar to curve (a) in figure 3. The spectra of 5.4 MeV Si implanted HOC-Si annealed at 400 °C (curve (b)) or 550 °C (curve (c)) are depicted in figure 8. The spectrum from the as-implanted sample (curve (a)) is also included for comparison. Due to the low O and C contents in the LOC-Si samples, the corresponding spectra (curves (c) and (d) in figure 7) do not show the presence of the VO centre nor that of the C related peaks. Furthermore, curves (a) and (c) in figure 7 clearly demonstrate that EHe203 is introduced in both HOC- and LOC-Si. It can, therefore,

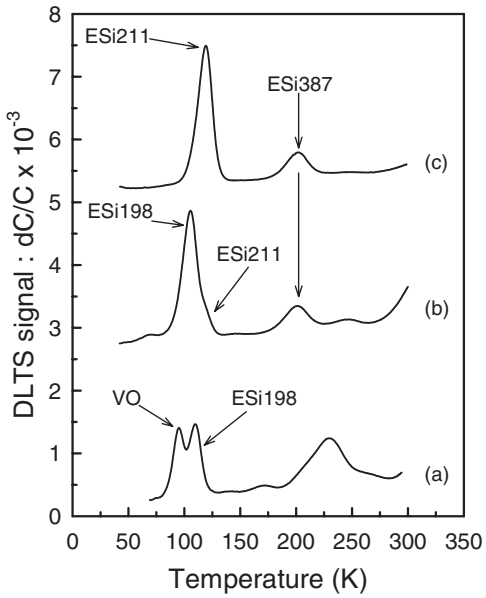

Figure 8. DLTS spectra from HOC n-type Si implanted with 5.4 MeV $^{28}Si^{4+}$ (curve (a)), and samples implanted and annealed at 400 or 550 °C (curves (b) and (c), respectively).

be concluded that EHe203 is a defect that does not involve C or O impurities. A comparison between the spectra in figure 7 further demonstrates that a defect ESi198, observed in both LOC- and HOC-Si, peaks at nearly the same temperature as EHe203. In addition, figures 4 and 8 show that the annealing behaviour of ESi198 is similar to that of EHe203. Hence, we conclude that EHe203 and ESi198 have the same structure. Using the results illustrated in figure 5, this latter conclusion can be extended to include ENe207 and EAr201. By comparing figures 1 and 7, it can also be said that the creation of the defect with a DLTS peak at ∼110 K (LIA frequency of 46 Hz) is independent of implantation species and strongly depends on the amount of energy deposited through elastic recoils. Hence, the results discussed above unambiguously reveal that EHe203, EAr201, and ENe207 constitute a family, N1, of defects structured similarly to ESi198 (figure 3 and table 1), which is not a point-like defect and is most probably intrinsic in nature (i.e. consisting of vacancy agglomerates).

Furthermore, the presence of the N1 defect in self-implanted HOC- and LOC-Si demonstrates unambiguously that this family of defects cannot arise from the chemical interaction between NGIs and defects created during nuclear energy deposition into elastic recoils. However, this discussion needs further qualification. Previous photoluminescence studies have revealed that the luminescence line corresponding to He incorporated into the I_1 defect is unstable above 300 °C, while the Ne related luminescence line anneals out at 350 °C [19]. The DLTS spectra depicted in figures 4–6 clearly demonstrate that EHe201 and ENe207 are thermally stable up to at least 450 °C, and cannot, therefore, be similar to the noble gas related defects observed by PL. Hence, the non-detection or low concentrations of $V_2^{2-/-}$ and $V_2^{-/0}$ in our 1 keV NGI bombarded samples cannot be explained by the incorporation of NGI into the divacancy.

The DLTS spectra of 5.4 MeV alpha particle irradiated HOC-Si (curves (a) and (c)) and LOC-Si (curves (b) and (d)) annealed at 350 and 500 °C are illustrated in figure 9. A defect Eα201 is produced after annealing at 350 °C (although a broadening of the VO centre on the

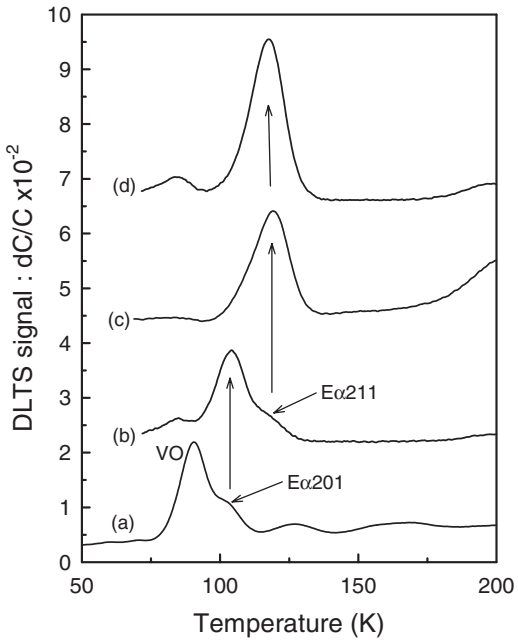

Figure 9. Isochronal annealing behaviour of the primary defects induced by 5.4 MeV alpha particle irradiation of HOC and LOC n-type Si. A defect Eα201 is observed to emerge after annealing at 300 °C in both samples (curves (a) and (b) for HOC- and LOC-Si, respectively), while curves (c) (HOC-Si) and (d) (LOC-Si) demonstrate that Eα211 is the dominant defect after annealing at 500 °C.

high temperature side begins at 300 °C). Although we have not studied the complete annealing kinetics of the defects, it would appear that the intensity of Eα201 increases at the expense of divacancies. Another interesting observation is that the intensity of Eα201 is larger in LOC-Si than in HOC-Si, which indicates that the presence of O in samples inhibits its formation by efficiently trapping vacancies. Furthermore, Eα201 is transformed into a defect Eα211 above 450 °C. The results shown in figure 9 also reveal that, similarly to that of EHe203, the formation of Eα201 does not involve C or O. Because of their similar peak positions (figures 1 and 9) and annealing behaviours (figures 4, 5 and 9) we propose that EHe203, ENe207, and EAr201 are structurally identical to Eα201. Since V_2 is known to be highly mobile above ∼300 °C [60, 61] and Eα201 grows at the expense of both VO and V_2, we conclude that Eα201 is due to defect reactions involving vacancies. This, together with the fact that very low concentrations of V_2 are present in our noble gas bombarded samples, implies that the N1 family of defects (i.e. EHe203, ENe207, and EAr201) is most probably due to higher order vacancy clusters (larger than V_2). Divacancies could be formed directly in collision cascades during 1 keV NGI bombardment of Si together with the formation of single vacancies. Combinations of V_2 and V can then give rise to complex vacancy clusters. Some of the single vacancies are efficiently trapped by interstitial O to form the VO centre.

Our annealing studies (figures 4, 5) further demonstrate that secondary defects are created by annealing the 1 keV NGI bombarded samples above 450 °C. Because of their similar peak positions and annealing behaviours, we propose that EHe211, ENe214, and EAr219 form a family of similarly structured defects (i.e. the N3 family of defects). It is seen from figures 4 and 5 that this family of secondary defects is introduced at the expense of the N1 family of defects, and the family of defects that is constituted by EHe584, ENeX, and ENeY. Figure 6

reveals that the annealing properties of EHe203 and EHe584 are similar. This, together with the fact that the secondary defects (N3) have a high thermal stability, suggests that they are due to complexes involving vacancy clusters larger than those responsible for the N1 defects. The possibility of NGI becoming incorporated into these higher order (secondary) vacancy clusters can be excluded because similar defects are detected in MeV self-implanted and alpha particle irradiated samples after annealing. Furthermore, the presence of EAr219 in unannealed 1 keV Ar ion bombarded HOC-Si (figure 1(d)) suggests that vacancy clusters larger than those responsible for EAr201 are produced when the nuclear energy loss becomes significant. The DLTS spectrum of 1 keV He ion bombarded LOC-Si (curve (c) of figure 7) features a prominent peak with an energy level at $E_C - 0.554$ eV which is thermally stable up to $\sim$500 °C. This level is not predominant in our low energy ion bombarded HOC-Si (curve (b) of figure 1) and has been found to be stable up to only $\sim$200 °C in 75 keV He implanted Si containing O [62].

3.1.3. Electric field assisted electron emission kinetics. It has been suggested that the sensitivity of the emission rate of a defect to an externally applied electric field can be used to probe the nature (donor or acceptor) and range of a defect potential [63, 64]. In particular, the range of the defect potential well is able to distinguish between point-like defects and larger defect clusters. In this section we discuss the electric field assisted electron emission kinetics of defects EHe203 (N1), EHe211 (N3), and EHe584, and demonstrate that the potential ranges associated with EHe203 and EHe211 are consistent with the above conclusion that they are complex defect clusters.

The emission rate of EHe584 shows virtually no electric field dependence. We have observed a variation of 5% (within experimental error) in its value after changing the electric field from 3×10^4 to 9×10^4 V cm^{-1}. The Poole–Frenkel effect has been widely used in the past to unambiguously determine whether a defect was of donor or acceptor type. It has, however, been demonstrated in a previous study [65] that short range perturbations to the long range Coulombic tail, such as an energy barrier to carrier capture, could dramatically decrease the effect of externally applied electric fields on Coulombic centres. Therefore, a null effect for the Poole–Frenkel effect does not unambiguously determine the defect type. Since the emission properties of EHe584 are electric field independent, and do not follow the Poole–Frenkel formalism, this defect is proposed to be of acceptor type.

Both EHe203 and EHe211 exhibit electric field enhanced electron emission rates, although the effect is much more pronounced for the former defect. We have previously shown that neither of these two defects behaved according to the one dimensional Poole–Frenkel formalism for a single charged defect [31]. In contrast to the Coulombic well, a spherically symmetric square well potential (radius b) gives rise to a more rapid variation of emission rate with electric field [66, 67]. A potential well that may be geometrically more realistic than the square well is the Gaussian well (depth V_0 and characteristic width α) [64, 68]. Given that the electron emission kinetics of EHe203 and EHe211 could not be explained using the Coulombic well model, we have instead employed the square and Gaussian well models.

Curve (b) in figure 10 (solid curve) shows that a square well with $b = 57$ Å gives a reasonable fit to the experimental data for EHe203. The depth of the square well has been assigned by assuming that the measured thermal activation energy of the trapped electron is the ground bound state energy in the well [69]. The effect of varying the dimension of the square well is demonstrated by curves (a) and (c). When fitting the Gaussian potential model to the experimental data of EHe203, values of 20 Å and 0.30 eV for α and V_0 ($E_T = 0.197$ eV), respectively, (cross-haired diamonds in figure 10) give an identical fit to the square well model with $b = 57$ Å. In this case, the trapped electron is not in the ground bound state in the potential well. For EHe211 (figure 11), a value of $b = 40$ Å for a square well of depth 0.35 eV gives a

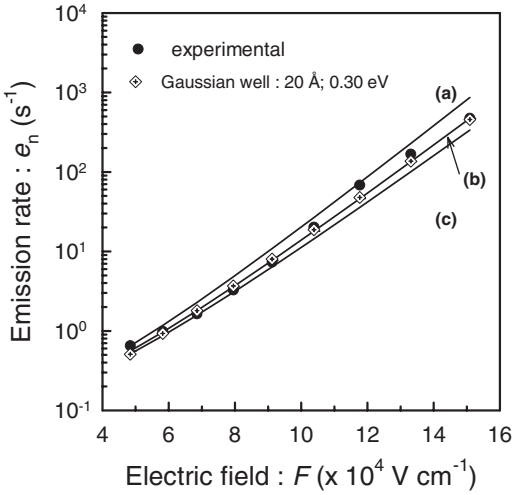

Figure 10. Modelled curves for a square well with three different dimensions for EHe203 (solid curves). A value of $E_T = 0.185$ eV was used for curves (a)–(c) while the values of b were 60, 57, and 55 Å, respectively. The solid circles represent the experimental data for EHe203 at 85 K. The cross-haired diamonds (overlap with curve (b)) show that the experimental emission rate can also be simulated using the Gaussian potential model for $\alpha = 20$ Å, $V_0 = 0.30$ eV, and $E_T = 0.197$ eV.

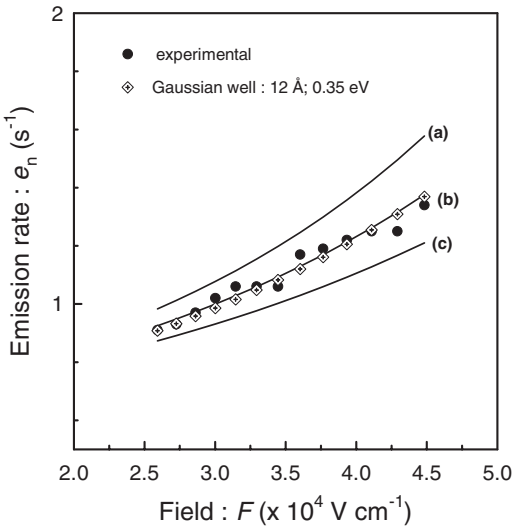

Figure 11. Modelled curves for a square well with three different dimensions for EHe211 (solid curves). Values of $E_T = 0.197$ eV and $\sigma_a = 3.2 \times 10^{-16}$ cm^2 were used for curves (a)–(c) while the values of b were 45, 40, and 35 Å, respectively. The solid circles represent the experimental emission rate for EHe211 at 100 K. The cross-haired diamonds (overlap with curve (b)) demonstrate that the experimental emission rate can also be simulated using the Gaussian potential model for $\alpha = 12$ Å, $V_0 = 0.35$ eV, and $E_T = 0.198$ eV.

reasonable fit to the experimental data (curve (b)). The influence of changing the radius of the square well is illustrated by curves (a) and (c). Similarly to those for EHe203, the experimental data for EHe211 could also be quite well fitted using the Gaussian well model. In this case,

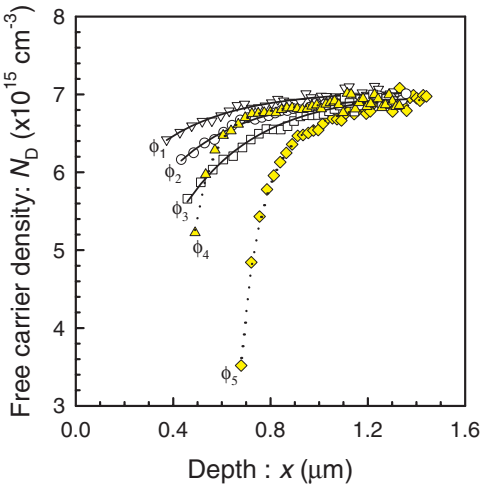

Figure 12. Free carrier profiles of 7.5 keV H implanted n-type Si at fluences $\phi_1 = 10^{11}$ H cm^{-2}, $\phi_2 = 10^{12}$ H cm^{-2}, $\phi_3 = 10^{13}$ H cm^{-2}, $\phi_4 = 10^{14}$ H cm^{-2}, and $\phi_5 = 10^{15}$ H cm^{-2}. The solid and broken curves through data points are fits to equation (1).

the dimensions of the Gaussian well are $\alpha = 12$ Å and $V_0 = 0.35$ eV ($E_T = 0.198$ eV) (cross-haired diamonds in figure 11). Since both types of well may give identical results, we have rationalized our choice for the square potential well model by opting for the solution requiring the least number of fitting parameters.

Since the ranges of potentials for point-like defects usually extend over only a few atomic spacings ($b < 10$ Å) [69], the experimental fits using the square potential well are in good agreement with the earlier proposition that EHe203 and EHe211 are complex vacancy clusters. On the basis of the above discussion, one may argue that the dimensions of the potential well associated with EHe211 ought to be larger than for that of EHe203. We point out here that the square well formalism does not account for defect charge states larger than one [67]. Hence, we propose that the larger potential range of EHe203 may be due to its higher charge state as compared to EHe211.

3.2. 7.5 keV H ion implanted n-type Si

We now discuss the changes in the electrical properties of n-type Si following 7.5 keV H ion implantation at different fluences. It is shown that the extent of free carrier compensation is closely related to the relative creation of the VP pair and the VO–H complex.

3.2.1. Free carrier compensation. Figure 12 illustrates the variation of free carrier concentration, N_D, determined from C–V measurements, as a function of low energy hydrogen ion fluence, ϕ. The hydrogen ion bombardment significantly reduces N_D within the first micron below the Si surface, and the extent of free carrier compensation, ΔN_D, exhibits two distinct ion fluence regimes. We have simulated the free carrier concentration by assuming the presence of two electron trapping centres with surface concentrations N_{T_i} ($x = 0$) ($i = 1, 2$), and characteristic decay lengths, λ_i ($i = 1, 2$). The spatial variation of $N_D(x)$ is expressed as

$$N_D(x) = N_D(\infty) - N_{T_1}(0)\exp(-x/\lambda_1) - N_{T_2}(0)\exp(-x/\lambda_2), \qquad (1)$$

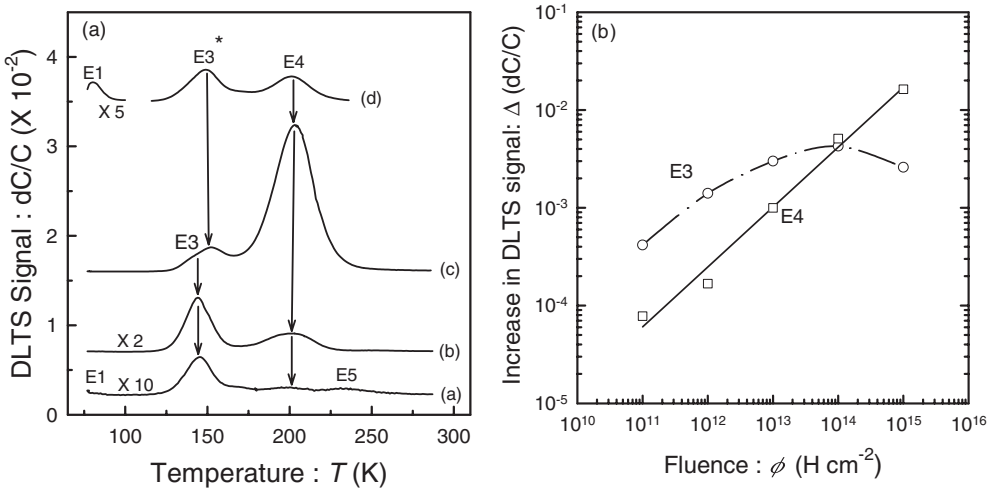

Figure 13. Panel (a) shows DLTS spectra from samples implanted with 10^{11}, 10^{13}, and 10^{15} H cm^{-2} (curves (a), (b), and (c), respectively); spectrum (d) is from a sample implanted with 10^{15} H cm^{-2} and subsequently annealed under zero bias at 155 °C for 20 min. Panel (b) shows the fluence dependence of the variation of the peak intensities of E3 and E4.

where $N_D(\infty) = 6.9 \times 10^{15}$ cm^{-3} is the free carrier concentration in the unimplanted sample. The solid and broken curves through the data points in figure 12 are fits to equation (1), and the values of the fitting parameters are listed in table 4. The two distinct fluence regimes are as follows:

(1) for $\phi \leqslant 1 \times 10^{13}$ H cm^{-2}, just one electron trap with diffusion length $\lambda_1 \sim 0.29$–0.31 μm is sufficient to explain the measured free carrier compensation, and
(2) for $\phi \geqslant 1 \times 10^{14}$ H cm^{-2}, an additional electron trap with a much shorter diffusion length $\lambda_2 \sim 0.070$–0.075 μm is required to account for ΔN_D.

The free carrier profiles in figure 12 have Debye uncertainties ranging from ∼51 nm (1×10^{11} H cm^{-2}) to ∼69 nm (1×10^{15} H cm^{-2}) associated with them [31], and are sufficiently low to be neglected here.

3.2.2. DLTS analysis. The range and energy deposited in elastic recoils of the 7.5 keV hydrogen ions were obtained from the binary collision code MARLOWE [70], as a function of their incident angle relative to a principal channelling axis, i.e. ⟨100⟩ [31]. Simulations have shown that the range of hydrogen ions and their energy loss in elastic recoils are within the zero bias depletion region (∼0.3 μm) of Schottky diodes in the worst case scenario of hyperchannelling (i.e. channelling angle $\Psi = 0°$) [31]. The results shown in figure 1 clearly establish, in conjunction with MARLOWE simulations [31], that the defects generated within the top ∼0.25 μm of samples migrated beyond 1 μm below the surface. MARLOWE was not used to obtain estimates of vacancy distributions since the simulations did not account for the vacancy/interstitial recombination. We have, therefore, used the binary code simulations to obtain the depth distributions of vacancies and hydrogen ions only.

Figure 13(a) shows DLTS spectra taken from samples implanted with 10^{11} H cm^{-2} (curve (a)), 10^{13} H cm^{-2} (curve (b)), and 10^{15} H cm^{-2} (curve (c)). The volume between the edge of the zero bias depletion region and ∼1.2 μm for each sample was probed by

Table 4. A list of the fitting parameters used for obtaining curves in figure 12.

Fluence, ϕ_1 (H cm^{-2})	$N_{T_1}(0)$ (10^{15} cm^{-3})	λ_1 (μm)	$N_{T_2}(0)$ (cm^{-3})	λ_2 (μm)
10^{11}	2.14	0.305	—	—
10^{12}	3.67	0.295	—	—
10^{13}	6.15	0.310	—	—
10^{14}	1.57	0.310	1.48×10^{18}	0.070
10^{15}	9.11	0.310	2.04×10^{19}	0.075

adjusting the reverse bias, V_r, and the filling pulse, V_p. Spectrum (d) will be discussed later. The results are treated semi-quantitatively because of the free carrier compensation in excess of 10% for the highest fluence. Electron traps E1 ($\sim E_C - 0.17$ eV), E3 ($\sim E_C - 0.28$ eV), E4 ($\sim E_C - 0.43$ eV), and E5 ($\sim E_C - 0.48$ eV) are introduced at the lowest dose (curve (a)). A defect E3* which overlaps with E3 is observed at the highest fluence. E1 is identified as the VO centre [52–55], while the interaction between the VO centre and H produces the VO–H complex, E3 [71–73]. E5 has previously been identified as another H related complex [73]. The superposition of the VP centre, the singly negative charge state of the divacancy, $V_2^{-/0}$, and possibly the interstitial carbon–substitutional phosphorus, C_iP_s, complex usually gives rise to E4 [73]. It is also worth noting that the acceptor levels of VH and V_2H have activation enthalpies indistinguishable from those of $V_2^{-/0}$ and the VP centre [74].

Figure 13(b) shows the variation in the peak intensities of the prominent defects E3 (excludes any contribution from E3*) and E4 as a function of hydrogen ion fluence. The peak intensity of E4 increases linearly with the increasing fluence, whereas that of E3 shows a maximum at $\phi_4 = 10^{14}$ H cm^{-2}. This fluence dependence for the creation of E3 and E4 is in semi-quantitative agreement with the two distinct free carrier compensation regimes in figure 12 and table 4. At the lower fluences, migrating single vacancies are efficiently trapped by O_i to form the VO centre [55], which then complexes with mobile hydrogen to form VO–H [71–73]. The mobile VO centre may also react with O_i to form the electrically neutral VO_2 pairs [73]. With the increasing fluence the formation of VO–H becomes limited by both the consumption of the fixed concentration of O_i in samples and the formation of electrically neutral VO_2 and VO–H_2 complexes [73]. An estimation made from the results in figure 13(b) shows that the concentration of E3 cannot account for the observed free carrier reductions for $\phi \leqslant 10^{13}$ H cm^{-2}. This is explained by the fact that a dominant fraction of VO pairs are already deactivated into VO–H_2 complexes in the H-rich environment.

Spectrum (d) in figure 13(a) is taken from a sample implanted with 10^{15} H cm^{-2} and subsequently annealed at 155 °C for 20 min under zero bias. Annealing at this modest temperature removes ~85% of E4, and we therefore exclude dominant contributions of $V_2^{-/0}$ and $V_2H^{-/0}$ to E4. The annealing behaviour of E4 is typical of the VP pair [72, 73, 75]. The predominance of the VP pair is also expected in Cz samples with resistivity <1 Ω cm [76]. Hence, our results show that O_i is a more efficient trap for mobile single vacancies than P dopant atoms. The dominance of P trapping of vacancies becomes efficient when the reservoir of O_i is consumed at the higher hydrogen fluences (i.e. above 1×10^{14} H cm^{-2}). The VP pair is more effective in consuming free electrons from the conduction band than the VO pair, since the formation of the former removes two electrons as opposed to one for the latter. Therefore, formation of VO–H is dominant for $\phi \leqslant 10^{13}$ H cm^{-2}, whereas VP becomes the dominant defect for $\phi \geqslant 10^{14}$ H cm^{-2}. The fluence dependence of the creation of VO–H and VP is well correlated with two distinct regimes for the free carrier compensation in low energy hydrogen ion implanted samples.

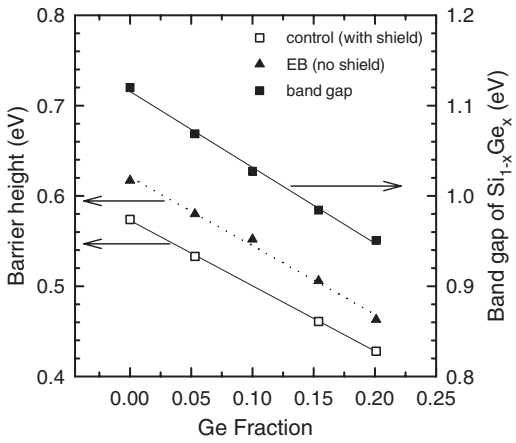

Figure 14. Variation of barrier height as a function of Ge fraction for Sc SBDs on p-type $Si_{1-x}Ge_x$ strained films by EBE with (solid line) or without shielding of the samples from stray electrons originating at the filament (dotted line). The band gap change is also given [76].

3.3. Processing of strained p-type $Si_{1-x}Ge_x$ epitaxial layers with low energy ions

We now turn our attention to the electrical properties of defects created in low energy ion irradiated $Si_{1-x}Ge_x$ epitaxial layers. First, the electrical properties of defects created in strained p-type layers during EBE of Sc contacts to form Schottky diodes followed by those created by sputter etching in a Ar plasma are reviewed. The second experiment was limited to samples with $x = 0$ and 0.05 only.

3.3.1. EBE induced defects in strained p-type $Si_{1-x}Ge_x$ epilayers. The defects created in epilayers following EBE of Sc Schottky contacts are discussed now. It is known that defects are created in the near-surface region of semiconductors during the fabrication of SBDs using EBE [46, 47]. These low energy particle induced defects are usually created within the depletion layer, which is not readily probed by capacitance spectroscopy techniques. In such cases, DLTS relies on the diffusion of defects outside the zero bias depletion layer width. Since the current–voltage (I–V) technique relies on the transfer of charge across the barrier between the semiconductor and the metal contact, it exhibits extreme sensitivity to the near-surface modification of the semiconductor. Hence, I–V measurements may provide complementary information to DLTS concerning the ion induced modification of the electrical properties of the semiconductor.

Figure 14 illustrates the variation of the Schottky barrier height and the band gap of strained $Si_{1-x}Ge_x$ [77] as a function of the Ge mole fraction, x. The values of the barrier height were extracted from the reverse current (at -1 V) rather than from the forward characteristic curve according to the thermionic emission theory because of the increasingly nonlinear character of the forward curves with increasing x (i.e. decrease in band gap) [39]. The decrease in barrier height with the increasing Ge mole fraction is related to the decrease in band gap of strained $Si_{1-x}Ge_x$ epilayers, and is consistent with previously reported results in the literature [78]. Furthermore, the barrier heights of diodes fabricated with the shield in place are consistently lower (by $\sim$40 meV) than those of diodes deposited without the shield. This result is consistent with the generally accepted proposition that low energy processing introduces donor-type defects in the near-surface region of the semiconductor material [79, 80], which results in

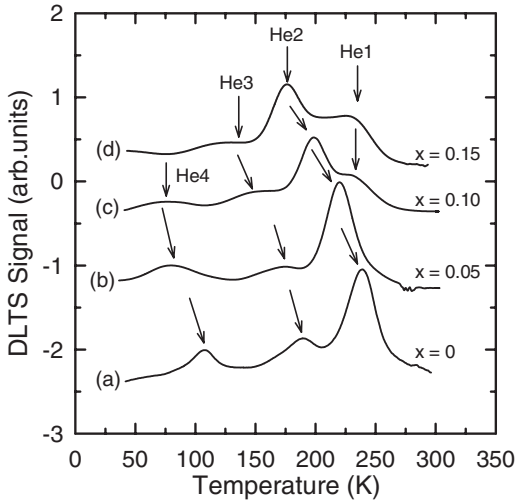

Figure 15. DLTS spectra of Sc SBDs deposited by EBE on p-type $Si_{1-x}Ge_x$ strained films. Curves (a)–(d) are for diodes fabricated on epilayers with $x = 0$, 0.053, 0.1, and 0.15, respectively. All spectra were recorded at a lock-in frequency of 46 Hz.

Table 5. Electronic properties of hole traps He1 and He2 introduced during EBE of Sc on epitaxially grown p-type $Si_{1-x}Ge_x$/Si.

Defect	Ge fraction (x)	E_T (eV)	σ_a (10^{-14} cm^2)	T_{peak} [a] (K)
He2	0	0.53	9.4	242
	0.053	0.47	5.1	222
	0.1	0.40	2.4	200
	0.15	0.35	2.4	176
He1	0.1	0.51	8.1	236
	0.15	0.50	9.6	232

[a] The peak temperature at a lock-in amplifier frequency of 46 Hz, i.e. a decay time constant of 9.23 ms.

increase or decrease in the barrier height of diodes fabricated on p- or n-type substrates, respectively. A generalized model concerning the increase in barrier height of diodes fabricated on low energy ion processed p-type semiconductors can be found in [81].

This leads us into the discussion of defects created in the strained p-type $Si_{1-x}Ge_x$ epilayers during EBE of Sc SBDs. Figure 15 illustrates the DLTS spectra taken from diodes fabricated without shielding the semiconductor surfaces from stray electrons originating from the filament. No defects are detected in samples shielded from stray electrons [34, 35]. EBE of Sc SBDs introduces a prominent hole trap, He2, in all samples, as well as minor traps He1, He3, and He4. The electronic properties of He1 and He2 are summarized in table 5. It should be noted that the peak temperatures of He1 and He2 in table 5 are higher than in figure 15, because the 'signatures' of these defects were determined under low electric field conditions, while spectra in figure 15 were recorded using forward bias filling pulses (i.e. high electric field conditions) in order to probe a volume as close to the semiconductor surface as possible [34]. The difference between the peak positions of defects in figure 15 and table 5 indicates that the hole emission properties of He1 and He2 are enhanced by an electric field. With the exception of that of He1, the peak positions of defects shift toward the lower temperatures with increasing

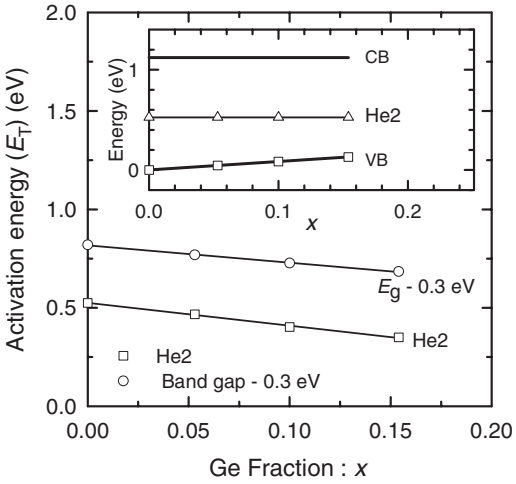

Figure 16. Variation of the $Si_{1-x}Ge_x$ band gap (solid circles) and the activation energy of the most prominent defect He2 (open squares) detected in EBE deposited Sc SBDs on p-type $Si_{1-x}Ge_x$ strained films as a function of the Ge fraction. The correlation between the change in activation energy of He2 and the change in valence band relative to Si with the Ge content is shown in the inset.

Ge mole fraction. The fact that the energy position of He1 ($\sim E_V + 0.50$ eV) is independent of x suggests that it is pinned to the valence band. Theoretical modelling has indicated that the major part of the variation of the band gap of $Si_{1-x}Ge_x$/Si heterostructures is contained in the valence band, VB [82].

The variation of the energy position of trap He2 in the band gap (open squares) is plotted in figure 16 as a function of the Ge content. The variation of the band gap as given in [77] is plotted with solid circles. The energy position of He2 is closely related to the band gap of the strained $Si_{1-x}Ge_x$ epilayer, and a linear dependence between the two parameters can be established. Reference [34] reveals that He2 in $Si_{1-x}Ge_x$ is the same defect as observed in p-type Si (i.e. $x = 0$). As shown in the inset in figure 16, the energy position of He2 is pinned in the band gap relative to the conduction band, CB, edge. This result may indeed reinforce the theory that the main part of the band gap variation in $Si_{1-x}Ge_x$/Si heterostructures is contained in the VB [82]. This discussion does not extend to He3 and He4 since their 'signatures' could not be determined accurately over the entire range of x.

3.3.2. Defects in Ar ion sputter etched strained p-type $Si_{1-x}Ge_x$ epilayers. SBDs were fabricated on control samples by shielding epilayers from stray electrons emanating from the filament during EBE of Ti contacts. The DLTS spectra taken from control samples, shown by curves (a) and (b) for $x = 0$ and 0.05, respectively, in figure 17, reveal that no defects were present in epilayers prior to sputter etching. The defects created by Ar plasma sputtering are illustrated by curves (c) and (d) for $x = 0$ and 0.05, respectively. The defects have been labelled HP1–HP6, with 'H' standing for hole trap and 'P' for plasma etching related defect. Defects created in Si (i.e. $x = 0$) are more clearly resolved than those created in $Si_{0.95}Ge_{0.05}$, most probably because of a broad background and a skewed baseline in the latter sample. The 'signatures' of the defects as determined from Arrhenius plots [36] are summarized in table 6. Most of the defects created in plasma etched Si are readily identified with other defects already reported in the literature. For instance, HP1 has a similar 'signature' to a defect, as yet of

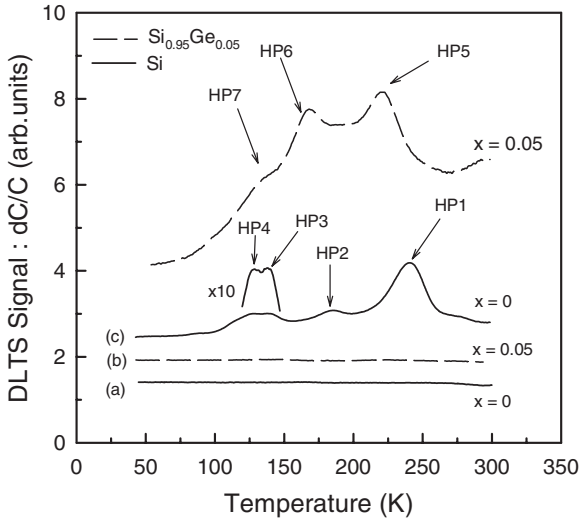

Figure 17. DLTS spectra of Ar plasma sputter etched p-type $Si_{1-x}Ge_x$. Curves (a) and (c) are for $x = 0$, while curves (b) and (d) are for $x = 0.05$. All spectra were recorded at a lock-in frequency of 46 Hz. Curves (a) and (b) are from the control samples.

Table 6. Electronic properties of hole traps introduced in Ar plasma sputter etched epitaxially grown p-type $Si_{1-x}Ge_x$/Si.

Defect	Ge fraction (x)	E_T (eV)	σ_a (cm^2)	T_{peak} [a] (K)
HP1	0	0.55	3.8×10^{-13}	241
HP2	0	0.39	5.4×10^{-14}	189
HP3	0	0.25	2.3×10^{-15}	139
HP4	0	0.22	9.5×10^{-16}	133
HP5	0.05	0.50	4.6×10^{-13}	221
HP6	0.05	0.35	2.2×10^{-14}	174

[a] The peak temperature at a lock-in amplifier frequency of 46 Hz, i.e. a decay time constant of 9.23 ms.

unknown structure, reported in [83, 84]. HP3 and HP4 are commonly attributed to the B–O centre [85] and the divacancy [86]. The 'signature' of HP2 is similar to that of the defect H(0.40) reported to occur in plasma etched Czochralski grown p-type Si [15] and is assigned to the C–O pair [87].

Figure 18 compares the defects created in $Si_{0.95}Ge_{0.05}$ by (a) Ar sputter etching, (b) EBE of Ti without shielding of stray electrons (see section 3.3.1), and (c) 5.4 MeV alpha particle irradiation. It is quite obvious that HP5 is similar to Heb and Hal5. It can be seen from table 6 that the peak positions (and energy positions in band gap) of HP5 and HP6 detected in p-type $Si_{0.95}Ge_{0.05}$ shift toward the lower temperatures relative to the peak positions of hole traps HP1 and HP2 in p-type Si, respectively. The composition related change in the activation energies of the two defects (∼47 meV) is virtually the same as the corresponding change in the band gap (∼50 meV) for a change in x from 0 to 0.05 [36]. Following the argument outlined in the previous section, it can be concluded that HP1 and HP2 detected in p-type Si are identical to HP5 and HP6 observed in $Si_{0.95}Ge_{0.05}$, respectively. This situation is illustrated in figure 19. Furthermore, HP1/HP5 (figure 17), Heb (figure 18), and Hal5 (figure 18) are similar to He2

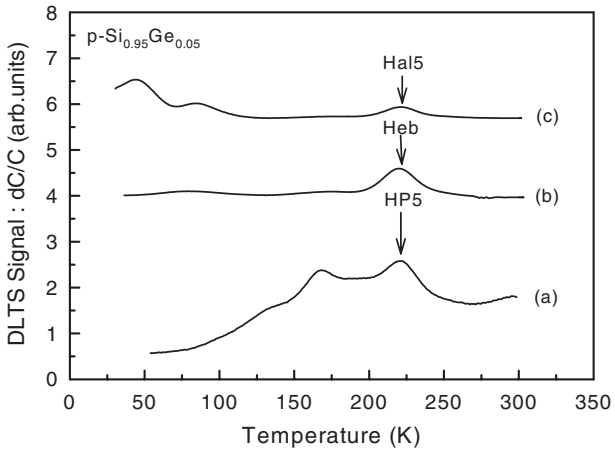

Figure 18. DLTS spectra of p-type $Si_{0.95}Ge_{0.05}$ after Ar plasma etching (a), after EBE of Ti SBDs without shielding (b), and after 5.4 MeV alpha particle irradiation (c). The spectra were recorded at a lock-in frequency of 46 Hz.

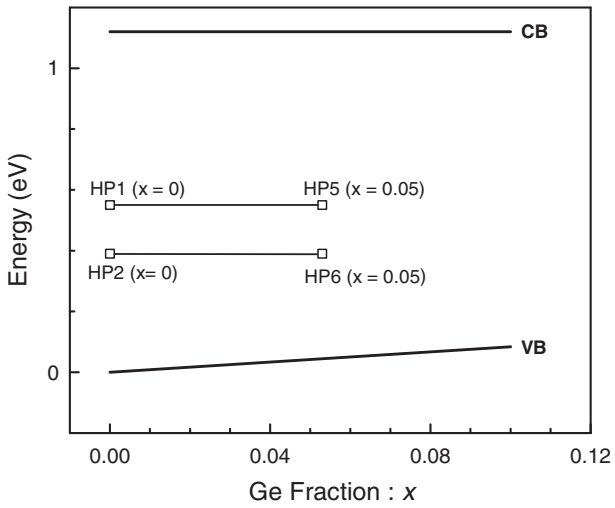

Figure 19. The correlation between the energy positions of the two major defects in Ar plasma etched p-type $Si_{1-x}Ge_x$ ($x = 0$ and 0.05) and the VB relative to Si and the Ge content.

discussed in the previous section. Its creation during MeV alpha particle irradiation suggests that it is a point-like defect.

4. Conclusions

We have reviewed our investigations of low energy NGI induced defects in epitaxially grown n-type Si, together with the defects created in Czochralski n-type Si by low energy hydrogen ion implantation. Also reviewed are defects created in strained p-type $Si_{1-x}Ge_x$ epilayers by electron beam evaporation of Schottky contacts or by plasma etching. The main findings and potential future studies can be summarized as follows.

4.1. Low energy NGI bombardment of n-type Si epilayers

DLTS was used in conjunction with isochronal annealing and electric field assisted electron emission rate experiments to investigate the electronic properties and annealing behaviour of the defects introduced in epitaxially grown n-type Si by 1 keV He, Ne, or Ar ion bombardment. Our results have shown that most of the defects introduced by the low energy NGIs are different from the point defects created by 5.4 MeV alpha particle irradiation. Divacancies are found to be present in very low concentrations in the 1 keV ion bombarded samples. On the basis of isochronal annealing experiments on low energy NGI bombarded n-type Si, as well as on samples irradiated with either 5.4 MeV alpha particles or 5.4 MeV Si ions, we have concluded that several new families of defects including N1 (EHe203, ENe207, and EAr201), N3 (EHe211, ENe214, and EAR219), and N4 (EHe584, ENeX, and EArY) introduced by NGI bombardment are most probably due to complex vacancy clusters *not involving* noble gas atoms. Another family of defects, N2 (EHe341, ENe347, and EAr310), could be related to the VO–H complex.

The N1 and N4 families of defects are stable up to $\sim$450 °C after which they anneal into the N3 family of secondary defects. The defects constituting the N3 family of defects are attributed to higher order vacancy clusters *not related* to NGI. This defect conversion has been studied in 1 keV He ion bombarded Si. By studying the electric field assisted electron emission kinetics of these defects, we have provided evidence for their relatively large potential ranges associated with these defects, and therefore their cluster-like nature. The increase in the ratios of the DLTS peak intensities of EHe203, ENe207, and EAr201, with respect to that of the VO centre, with increasing bombarding ion mass further demonstrates that, as expected, the concentration of complex vacancy clusters increases with increasing nuclear energy deposition in elastic recoils. EAr219 (i.e. the N3 family of defects) is detected in 1 keV Ar ion bombarded samples, suggesting that higher order vacancy clusters can be produced at room temperature. Finally, we have demonstrated that creations of the N1, N3, and N4 families of defects are not related to O and C impurities.

It is timely here to mention that the above studies have provided some insight into the properties of defects, most notably vacancy clusters, created in low energy NGI bombarded Si. However, more effort should be devoted in the future in order to further qualify and quantify the properties of these defects. For instance, a detailed characterization of the N4 family of defects is required, together with the comprehensive annealing kinetics (from isothermal annealing experiments) of the N1, N3, and N4 families of defects. Another very important set of experiments should cover the correlation between the creation of the N1 defect (i.e. Eα201) in 5.4 MeV alpha particle irradiated samples and the removal of vacancy related point defects, especially the divacancies, and, further, the creation of the N3 defect (i.e. Eα211) at the expense of the N1 defect. Yet another set of experiments could focus on the effect of hydrogenation of samples containing the N1–N4 family of defects, as well as the reversibility of any hydrogen passivation effects on these complex defects.

4.2. Low energy H ion implantation of n-type Si

DLTS was used to study the generation of E3, the VO–H complex, and E4, the VP pair, in 7.5 keV H implanted n-type Si at different fluences. Vacancies are produced within the top $\sim$0.25 μm of samples, and their subsequent migration and trapping by interstitial O and P dopant atoms produce the VO centre and VP pair up to depths exceeding 1 μm. The VO–H complex is formed by the reaction between the mobile VO centre and H. Formation of VO–H is dominant for $\phi \leqslant 10^{13}$ H cm^{-2}, whereas VP is the dominant defect for $\phi \geqslant 10^{14}$ H cm^{-2},

when the fixed reservoir of O_i is used up and the electrically inactive VO–H_2 complex is formed. The fluence dependence of the creation of E3 and E4 is well correlated with two distinct regimes for the free carrier compensation in implanted samples. Simulations show that two defects with characteristic decay lengths $\lambda_1 \sim 0.29$–0.31 and $\lambda_2 \sim 0.070$–0.075 μm are sufficient to explain our experimental data. Hence, the fluence dependence of free carrier compensation is well correlated with the relative creation of VO–H and VP defects.

4.3. Processing of strained p-type $Si_{1-x}Ge_x$ epilayers

Electron beam evaporation of Sc (or Ti) SBDs on unshielded $Si_{1-x}Ge_x$ epilayers creates electrically active hole traps He1–He4 in the semiconductor material. The SBDs fabricated without shielding have higher barrier heights compared to the control samples, and this can be explained by the presence of donor-type defects in the near-surface region of the exposed semiconductor. The change in the barrier height with Ge content gives the expected variation for the band gap for strained layers. Evidence is provided that He1 ($\sim E_V + 0.50$ eV) is pinned relative to the valence band edge, whereas the activation energy of He2 decreases with increasing Ge mole fraction (i.e. the energy position of He2 is pinned to the conduction band edge). Sputter etching using 0.4 keV Ar ions also creates defects in strained p-type $Si_{1-x}Ge_x$. The main defects HP1 and HP2 detected in p-type Si (i.e. $x = 0$) are also observed in p-type $Si_{0.95}Ge_{0.05}$, and their energy positions are pinned to the conduction band edge. HP1 is probably the same as He2 (an EBE induced defect), while HP2 is identified as the interstitial carbon–interstitial oxygen pair.

Acknowledgments

The authors are grateful for the financial support of the National Research Foundation, South Africa. Most of this work PNKD performed at the Department of Physics, University of Pretoria, Pretoria 0002, Republic of South Africa. PNKD also acknowledges the financial support of the Australian Research Council.

References

[1] Stavola M 1999 *Physica* B **273/274** 1
[2] Grimmeiss H G 1977 *Annu. Rev. Mater. Sci.* **7** 341
[3] Corbett J W, Karins J P and Tan T Y 1981 *Nucl. Instrum. Methods* **182/183** 457
[4] Zalm P C, van den Berg J A, van Berkum J G M, Bailey P and Noakes T C Q 2000 *Appl. Phys. Lett.* **76** 1887
[5] Lang D V 1974 *J. Appl. Phys.* **45** 3014
[6] Lang D V 1974 *J. Appl. Phys.* **45** 3023
[7] Kimerling L C 1981 *Defects in Semiconductors* (*Materials Research Society Proc.* vol 2) ed J Narajan and T Y Tan (New York: North-Holland) p 85
[8] Li G P and Wang K L 1983 *Solid State Electron.* **26** 825
[9] Pearton S J 1981 *Phys. Status Solidi* b **105** K19
[10] Lamp C D, Farmer J W and Meese J M 1984 *Rev. Sci. Instrum.* **55** 210
[11] Kamiura Y, Ishiga N and Yamashita Y 1997 *Japan. J. Appl. Phys.* **36** L1419
[12] Dobaczewski L, Gościński K, Żytkiewicz Z R, Bonde Nielsen K, Rubaldo L, Andersen O and Peaker A R 2002 *Phys. Rev.* B **65** 113203
[13] Dobaczewski L, Kaczor P, Hawkins I D and Peaker A R 1994 *J. Appl. Phys.* **76** 194
[14] Dobaczewski L, Gościński K, Bonde Nielsen K, Nylandsted Larsen A, Lundsgaard Hansen J and Peaker A R 1999 *Phys. Rev. Lett.* **83** 4582
[15] Awadelkarim O O, Gu T, Mikulan P I, Ditizio R A, Fonash S J, Reinhardt K A and Chan Y D 1993 *Appl. Phys. Lett.* **62** 958
[16] Balooch M, Moalem M, Wang W-E and Hamza A V 1996 *J. Vac. Sci. Technol.* A **14** 229

[17] Zhu S, Detavernier C, Van Meirhaeghe R L, Cardon F, Blondeel A, Clauws P, Ru G-P and Li N-Z 2001 *Semicond. Sci. Technol.* **16** 83
[18] Deenapanray P N K, Auret F D and Myburg G 1998 *J. Vac. Sci. Technol.* B **16** 1873
[19] Burger N, Thonke K, Sauer R and Pensl G 1984 *Phys. Rev. Lett.* **52** 1645
[20] Davis R J, Habermeier H-U and Weber J 1985 *Appl. Phys. Lett.* **47** 1295
[21] Minaev N S, Mudryi A V and Tkachev V D 1981 *Phys. Status Solidi* b **108** K89
[22] Sawyer W-D, Weber J, Nabert G, Schmalzlin J and Habermeier H-U 1990 *J. Appl. Phys.* **68** 6179
[23] Estreicher S K, Weber J, Derecskei-Kovacs A and Marynick D S 1997 *Phys. Rev.* B **55** 5037
[24] Estreicher S K, Hastings J L and Fedders P A 1997 *Appl. Phys. Lett.* **70** 432
[25] Tkachev V D, Mudryi A V and Minaev N S 1985 *Phys. Status Solidi* a **81** 313
[26] Deenapanray P N K, Auret F D, Ridgway M C, Goodman S A, Myburg G and Malherbe J B 1998 *J. Appl. Phys.* **84** 2565
[27] Deenapanray P N K, Perret N E, Brink D J, Auret F D and Malherbe J B 1998 *J. Appl. Phys.* **83** 4075
[28] Auret F D, Deenapanray P N K, Goodman S A, Meyer W E and Myburg G 1998 *J. Appl. Phys.* **83** 5576
[29] Deenapanray P N K, Auret F D and Myburg G 1999 *Nucl. Instrum. Methods* B **148** 300
[30] Deenapanray P N K, Meyer W E and Auret F D 1999 *Semicond. Sci. Technol.* **14** 41
[31] Deenapanray P N K 2002 *Appl. Phys. Lett.* **80** 1577
[32] Haller E E 1991 *Semicond. Sci. Technol.* **6** 73
[33] Pearton S J, Corbett J W and Shi T S 1987 *Appl. Phys.* A **43** 153
[34] Mamor M, Auret F D, Goodman S A and Myburg G 1998 *Appl. Phys. Lett.* **72** 1069
[35] Mamor M, Auret F D, Goodman S A, Myburg G, Deenapanray P N K and Meyer W E 1997 *Mater. Sci. Forum* **258–263** 115
[36] Mamor M, Auret F D, Willander M, Goodman S A, Myburg G and Meyer F 1999 *Semicond. Sci. Technol.* **14** 611
[37] Goodman S A, Auret F D, Nauka K and Malherbe J B 1997 *J. Electron. Mater.* **26** 463
[38] Goodman S A, Auret F D, Mamor M, Deenapanray P N K and Meyer W E 1997 *Mater. Sci. Forum* **258–263** 133
[39] Goodman S A, Auret F D, Mamor M and Greiner A 1998 *Appl. Phys. Lett.* **73** 256
[40] Ismail K, Chu J O and Meyerson B S 1994 *Appl. Phys. Lett.* **64** 3124
[41] Arienzo M, Iyer S S, Meyerson B S, Patton G L and Stork J M C 1991 *Appl. Surf. Sci.* **48** 377
[42] Iyer S S, Patton G L, Stork J M C, Meyerson B S and Harame D L 1989 *IEEE Trans. Electron Devices* **36** 2043
[43] Meyerson B S 2000 *IBM J. Res. Dev.* **44** 391
[44] Mooney P M 1996 *Mater. Sci. Eng.* **17** 105 and references therein
[45] Koester S J, Hammond R, Chu J O, Mooney P M, Ott J A, Perraud L, Jenkins K A, Webster S, Lagnado I and de la Houssaye P R 2001 *IEEE Electron Device Lett.* **22** 92
[46] Myburg G and Auret F D 1992 *J. Appl. Phys.* **71** 6172
[47] Christensen C, Petersen J W and Nylandsted Larsen A 1992 *Appl. Phys. Lett.* **61** 1426
[48] Kringhøj P and Nylandsted Larsen A 1995 *Phys. Rev.* B **52** 16333
[49] Lefevre H and Schultz M 1977 *Appl. Phys.* **12** 45
[50] Zohta Y and Watanabe M O 1982 *J. Appl. Phys.* **53** 1809
[51] Ziegler J F, Biersack J P and Littmark U 1985 *The Stopping and Range of Ions in Solids* vol 1, ed J F Ziegler (New York: Pergamon)
[52] Brotherton S D and Bradley P 1982 *J. Appl. Phys.* **53** 5720
[53] Kimerling L C, Asom M T, Benton J L, Drevinsky P J and Caefer C E 1989 *Mater. Sci. Forum* **38–41** 141
[54] Svensson B G, Jagadish C, Hallén A and Lalita J 1997 *Phys. Rev.* B **55** 10498
[55] Watkins G D 1991 Electronic structure and properties of semiconductors *Materials Science and Technology, a Comprehensive Treatment* vol 4, ed Schröter (Weinheim: VCH) p 105
[56] Abdullin Kh A, Mukashev B N, Tamendarov M F and Tashenov T B 1992 *MRS Symp. Proc.* **262** 1109
[57] Thompson D A and Walker R S 1978 *Radiat. Eff.* **36** 91
[58] Deenapanray P N K and Williams J S 1999 *MRS Symp. Proc.* **540** 121
[59] Schröter W, Kronewitz J, Gnauert U, Riedel F and Seibt M 1995 *Phys. Rev.* B **52** 13726
[60] Evwaraye A O and Sun E 1976 *J. Appl. Phys.* **47** 3776
[61] Svensson B G, Johnsson K, Xu D-X, Svensson J H and Lindström J L 1989 *Radiat. Eff. Defects Solids* **111/112** 439
[62] Erokhin Yu N, Ravi J, White C W and Rozgonyi G 1995 *Nucl. Instrum Methods* B **96** 223
[63] Bourgoin J C and Lannoo M 1983 *Experimental Aspects* (*Point Defects in Semiconductors* vol 2) (New York: Springer) pp 191–202
[64] Wang K L and Li G P 1983 *Solid State Commun.* **47** 233

[65] Buchwald W R and Johnson N M 1988 *J. Appl. Phys.* **64** 958
[66] Auret F D, Goodman S A and Meyer W E 1995 *Semicond. Sci. Technol.* **10** 1376
[67] Hartke J L 1968 *J. Appl. Phys.* **39** 4871
[68] Zhu Q S, Hiramatsu K, Sawaki N, Akasaki I and Liu X N 1993 *J. Appl. Phys.* **73** 771
[69] Walker J W and Sah C T 1973 *Phys. Rev.* B **8** 5597
[70] Robinson M T and Torrens I M 1974 *Phys. Rev.* B **9** 5008
[71] Johannesen P, Bech Nielsen B and Byberg J R 2000 *Phys. Rev.* B **61** 4659
[72] Deenapanray P N K 2001 *Physica* B **308–310** 190
[73] Pellegrino P, Lévêque P, Lalita J, Hallén A, Jagadish C and Svensson B G 2001 *Phys. Rev.* B **64** 195211 and references therein
[74] Bonde Nielsen K, Dobaczewski L, Goscinski K, Bendensen R, Andersen O and Bech Nielsen B 1999 *Physica* B **273/274** 167
[75] Nylandsted Larsen A, Christensen C and Petersen J W 1999 *J. Appl. Phys.* **86** 4861
[76] Svensson B G, Aboelfotoh M O and Lindström J L 1991 *Phys. Rev. Lett.* **66** 3028
[77] Dutartre D, Bremond G, Souifi A and Benyattou T 1991 *Phys. Rev.* B **44** 11525
[78] Nur O, Willander M, Turan R, Sardela M R Jr, Radamson H H and Hansson G V 1997 *J. Vac. Sci. Technol.* B **15** 241
[79] Fonash S J, Ashok S and Singh R 1981 *Appl. Phys. Lett.* **39** 423
[80] Auret F D, Goodman S A, Myburg G and Meyer W E 1992 *J. Vac. Sci. Technol.* B **10** 2366 and references therein
[81] Goodman S A, Auret F D, Deenapanray P N K and Myburg G 1998 *Japan. J. Appl. Phys.* **37** L10
[82] Van de Walle C G and Martin R M 1986 *Phys. Rev.* B **34** 5621
[83] Troxell B J 1983 *Solid State Electron.* **26** 539
[84] Giri P K, Dhar S, Kulkarni V N and Mohapatra Y N 1997 *J. Appl. Phys.* **81** 260
[85] Dombrovskii R R 1984 *Sov. Phys.—Semicond.* **18** 371
[86] Baliga B J and Evwaraye A O 1983 *J. Electrochem. Soc.* **30** 1916
[87] Vanhellemont J, Kaniava A, Simoen E, Trauwaert M A, Claeys C, Johlander B, Harboe-Sörensen R, Adams L and Clauws P 1994 *IEEE Trans. Nucl. Sci.* **41** 479